Bifurcation-aware optimization and robust synchronization of coupled laser diodes

Jonas Otten,* Jens Müller,† and Martin Mönnigmann‡
Automatic Control and Systems Theory, Ruhr-Universität Bochum, 44801 Bochum, Germany

(Received 18 May 2018; published 12 December 2018)

We interpret the problem of synchronizing multiple coupled laser diodes as a robust stabilization problem. We show that mathematical optimization, specifically constrained nonlinear programming, can be applied to identify stable and robust points of operation with optimal intensities. In contrast to existing methods, the method proposed here does not require multicriteria or Pareto-optimizations for a simultaneous treatment of optimality and robustness. It is based on enforcing a safe distance to manifolds of saddle-node and Hopf bifurcations (or generalizations thereof), where the distance can be chosen to reflect parametric uncertainties of the model or the system operation. While the method involves linearizations, it captures, in the same sense as bifurcation theory, the true nonlinear behavior of the system.

DOI: 10.1103/PhysRevE.98.062212

I. INTRODUCTION

Photon lifetimes, which determine the speed of dynamics in semiconductor lasers, are typically in the magnitude of a picosecond [1, p. 232]. Consequently, it is not trivial to control their stability properties. Moreover, semiconductor lasers can exhibit complex dynamical behavior since, among other reasons, the refractive index of the semiconductor depends on the carrier density. This distinguishes them from other lasers, especially in the presence of a second, external cavity. A laser model that is able to explain these experimental findings is the Lang-Kobayashi model [2].

There are many variations of the Lang-Kobayashi model available. It is, for example, possible to include carrier diffusion in the dynamical model, which increases the dimension of the state space [3] and, consequently, the computational effort of an analysis [4]. A common simplification assumes a linear relation of carrier density and modal gain [4–9].

Laser diodes are coupled for one of three reasons: to induce chaos to their dynamics, to electronically move the laser beam, or to achieve a greater output intensity than with a single laser diode. The first case exploits that two lasers might be in a mode where they synchronize with each other, even when they are operating chaotically [6,10]. The chaotic signal can, for example, be used as a carrier for secure communication [11]. The second reason to couple lasers is to electronically scan with a laser beam. If single arrayed lasers emit light with an electronically induced phase shift, their interference pattern is manipulated and the direction of the largest output intensity changes [12]. The last reason to couple lasers is overcoming the intensity limitations of single laser diodes. Scaling up the pump current as the energy source cannot increase the intensity of a single laser diode arbitrarily [1, p. 218].

The complex dynamics of semiconductor lasers have been studied extensively by bifurcation analysis. Laser diodes with phase conjugating external feedback [13] as well as conventional optical feedback [5,7,14,15] and semiconductor ring lasers [16] are just a few examples of interesting targets for bifurcation analysis.

The fast and complex dynamics of semiconductor lasers have motivated strategies for finding parameters that enable their stable open-loop operation. Kozyreff *et al.* [17,18] present a comprehensive analysis of coupled identical laser diodes and identify bifurcation manifolds that separate parameter space regions with different synchronization properties. Kozyreff *et al.* point out that these boundaries are, beyond their fundamental importance, of technological interest, because they can be used to find stable points of operation with large output power.

Several authors have applied methods from the field of mathematical optimization, such as nonlinear programming (see, e.g., Ref. [19]) and multicriteria or Pareto-optimization (see, e.g., Ref. [20]), to laser diodes. Mathematical optimization is an interesting alternative whenever a comprehensive analysis, for example a bifurcation analysis, is too difficult or time consuming. This may be the case if the number of parameters (such as adjustable pump currents) is large and cannot be reduced by exploiting symmetries, for example. Vanbiervliet *et al.* [21] propose an optimization method for the stabilization of nonlinear systems with delay and apply their approach to laser dynamics. They minimize the real part of the leading eigenvalue for external cavity mode solutions. Kouomou and Woafo [22] use a similar approach for the synchronization of laser diodes. Here, the leading eigenvalue real part is minimized to accelerate synchronization. Priyadarshi *et al.* [23] state and solve an optimization problem that achieves a fast convergence to a state of synchronization and an increased signal-to-noise ratio in coupled lasers. A minimization of leading eigenvalue real parts is also possible for uncertain delayed systems. Fenzi and Michiels [24] propose an optimization approach where stochastic parameter uncertainty is treated by minimizing the expected real part of the leading eigenvalue.

The optimization approaches in Refs. [21,24] include stability properties in their objective functions. Essentially, the

*jonas.otten@rub.de
†jens.mueller-r55@rub.de
‡martin.moennigmann@rub.de

objective function is used to push the eigenvalues as far to the left in the complex plane as possible. This is reasonable when it is the objective to converge to a steady state as fast as possible. However, while the distance of the leading eigenvalue to the imaginary axis is a good measure for stability and the rate of convergence, it is not a good measure for robustness. This difference between stability and robustness arises because eigenvalues are not uncertain themselves, but their uncertainty is caused by properties of the model such as uncertain parameters. The leading eigenvalue may, for example, be insensitive to the variation of the uncertain parameters. Another eigenvalue may be sensitive and therefore take the role of the leading eigenvalue under parameter variations. As a result, the distance to the imaginary axis of the leading eigenvalue for nominal parameters is not a measure for how large parameter variations may become before stability is lost. We propose to use the distance to the closest manifold of critical points in the parameter space as a measure for robustness (see Sec. II D). As a side effect, robustness requirements can be stated as constraints of a constrained nonlinear programming problem. Consequently, stability and robustness properties no longer need to be incorporated in the objective function. The objective function may therefore be used to state other criteria (such as laser intensity) without any need for Pareto-optimization or multicriteria optimization with weighting factors.

The proposed approach belongs to the class of normal vector methods [25]. Dobson [26] proposed using normal vectors on bifurcation manifolds to find the closest manifold, i.e., the bifurcation that can be caused by the smallest multidimensional parameter shift. This idea was adopted by Mönnigmann and Marquardt [25] to keep a predefined parametric distance from bifurcation manifolds during steady state optimization of systems governed by ordinary differential equations. There exist extensions of the normal vector method, to robust disturbance rejection [27], discrete time systems [28], delayed systems [29], and periodically operated systems [30]. In this contribution we extend previous results for delayed systems [31,32] to periodically operated systems with rotational symmetry and apply these methods to coupled lasers.

Section II first motivates why robust optimization methods are required for finding optimal open-loop stable modes of operation for laser diodes. Subsequently, the method proposed in this paper is introduced. A simple network of two coupled lasers serves as an example. More complex problems with up to ten nonidentical lasers and ten uncertain parameters are treated in Sec. III. Conclusions are given in Sec. IV.

II. ROBUST OPTIMIZATION OF COUPLED LASER DIODES

A. Laser model and coupling

All laser diodes in Secs. II and III are modeled by a Lang-Kobayashi model. The delay differential equation system reads

$$\frac{1}{\theta}\dot{E}(t) = (1+\mathrm{i}\alpha)\,n(t)E(t) + \eta\,\mathrm{e}^{\mathrm{i}\phi}\,E(t-\tau), \qquad (1a)$$

$$\frac{1}{\theta}\dot{n}(t) = \epsilon\{p - n(t) - [2n(t)+1]|E(t)|^2\}. \qquad (1b)$$

TABLE I. Model parameters for each laser diode as given in Ref. [15]. Coupled lasers have multiple coupling coefficients, therefore the value of η does not apply for laser networks. The pump current p is omitted, as it will be the optimization variable.

	Parameter	Numerical value
α	linewidth enhancement factor	4
η	coupling coefficient	0.005
ϕ	coupling phase	−2
τ	coupling delay	rescaled: $100\frac{1}{\theta}$
ϵ	carrier relaxation time	0.005

We added the time scaling factor $\theta = 1000$ to the standard model [5,7,8,33] for more convenient time scales in trajectory plots later on. Parameters are given in Table I.

We couple the laser diodes symmetrically as shown in Fig. 1. Both lasers receive their own feedback signal and the coupling signal emitted by the other laser. These signals interfere additively [6,17].

The delay differential equation system for this laser network reads

$$\frac{1}{\theta}\dot{E}_1(t) = (1+\mathrm{i}\alpha)n_1(t)E_1(t) + \sum_{k=1}^{2}\eta_{1k}\mathrm{e}^{\mathrm{i}\phi}E_k(t-\tau), \qquad (2a)$$

$$\frac{1}{\theta}\dot{n}_1(t) = \epsilon\{p_1 - n_1(t) - [2n_1(t)+1]|E_1(t)|^2\} \qquad (2b)$$

$$\frac{1}{\theta}\dot{E}_2(t) = (1+\mathrm{i}\alpha)n_2(t)E_2(t) + \sum_{k=1}^{2}\eta_{2k}\mathrm{e}^{\mathrm{i}\phi}E_k(t-\tau) \qquad (2c)$$

$$\frac{1}{\theta}\dot{n}_2(t) = \epsilon\{p_2 - n_2(t) - [2n_2(t)+1]|E_2(t)|^2\}. \qquad (2d)$$

The sum in Eq. (2a) represents the electrical field that is fed into laser 1. The sum in Eq. (2c) is motivated accordingly. Since light emitted by each laser diode has to be fed back into two lasers, it must be split. We use the coupling coefficients $\eta_{jk} = 0.0025$ for $j,k = 1,2$, which obey the relation $\eta = \eta_{1k} + \eta_{2k}$ for both laser diodes, i.e., $k = 1,2$.

It is convenient to analyze the synchronized state of the coupled lasers in a coordinate frame that rotates with the common frequency of the two lasers. Rotating coordinate frames are established in the analysis of single lasers [2,5,7,14,15]. This change of coordinates Eq. (3) results in an eigenvalue $\lambda = 0$, which, however, is known not to have any impact on stability [7,21,34]. Substituting the rotating coordinates

$$E_j(t) = A_j(t)\,\mathrm{e}^{\mathrm{i}\Omega t}, \qquad (3)$$

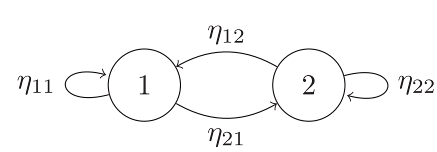

FIG. 1. Coupling structure of two coupled lasers.

where Ω is the angular frequency of rotation, into Eq. (2) yields

$$\frac{1}{\theta}\dot{A}_1(t) = -\mathrm{i}\Omega A_1(t) + (1+\mathrm{i}\alpha)n_1(t)A_1(t) + \sum_{k=1}^{2}\eta_{1k}\mathrm{e}^{\mathrm{i}(\phi-\Omega\tau)}A_k(t-\tau), \tag{4a}$$

$$\frac{1}{\theta}\dot{n}_1(t) = \epsilon\{p_1 - n_1(t) - [2n_1(t)+1]|A_1(t)|^2\}, \tag{4b}$$

$$\frac{1}{\theta}\dot{A}_2(t) = -\mathrm{i}\Omega A_2(t) + (1+\mathrm{i}\alpha)n_2(t)A_2(t) + \sum_{k=1}^{2}\eta_{2k}\mathrm{e}^{\mathrm{i}(\phi-\Omega\tau)}A_k(t-\tau), \tag{4c}$$

$$\frac{1}{\theta}\dot{n}_2(t) = \epsilon\{p_2 - n_2(t) - [2n_2(t)+1]|A_2(t)|^2\}. \tag{4d}$$

Steady states of Eq. (4) correspond to synchronized states of the coupled lasers, which implies that both lasers emit light with the same frequency Ω. Also, steady states of the coupled lasers Eq. (4) are equivalent to external cavity modes (ECMs) of single laser diodes. Therefore, an additional equation is necessary to resolve the phase indeterminacy [7]. We will use the phase condition

$$0 = \mathrm{Re}\{A_1\} - \mathrm{Im}\{A_1\}, \tag{5}$$

which was proposed by Verheyden *et al.* [4].

We abbreviate Eqs. (4) and (5) by

$$\dot{x}(t) = f(x(t), x(t-\tau_1), \ldots, x(t-\tau_m), p, \Omega), \tag{6}$$

$$0 = \varphi(x). \tag{7}$$

In Eq. (4) we have $n_x = 6$ states in a vector $x = [\mathrm{Re}\{A_1\}, \mathrm{Im}\{A_1\}, n_1, \mathrm{Re}\{A_2\}, \mathrm{Im}\{A_2\}, n_2]^T$, one delay τ, $n_p = 2$ uncertain parameters[1] in a vector $p = [p_1, p_2]^T$, and one algebraic variable Ω.

The synchronization condition above still allows the laser diodes to operate at different phase angles. Different phase angles might reduce the resulting intensity, when the oscillating outputs of the laser diodes interfere. However, the following results show that a laser network might reach its highest output while laser diodes operate at different phase angles, which is the case for asymmetric network topologies or when laser diodes have different pump current restrictions.

B. Naive optimization fails

Consider the problem of maximizing the intensity of two synchronized lasers by varying the pump currents p_1 and p_2. Assume all parameters are fixed and only p_1 and p_2 may be varied. This leads to the optimization problem

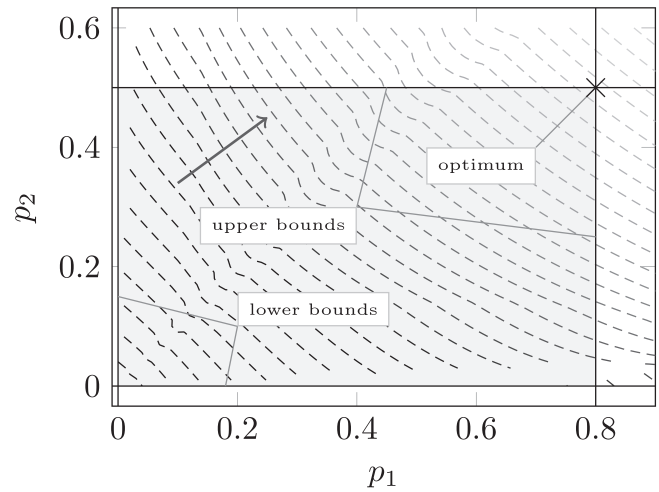

FIG. 2. The intensity is limited by the upper bounds of p_1 and p_2. Dashed lines are contour lines and represent the intensity, which ranges from 0 in the lower left corner to 2.9 in the upper right corner. The arrow points in the direction of higher intensities.

$$\min_{p_1,p_2} -|A_1 + A_2|^2, \tag{8a}$$

$$\text{s.t. } 0 = f(x, x, p, \Omega), \tag{8b}$$

$$0 = \varphi(x), \tag{8c}$$

$$p_1 \in [0, 0.8], \quad p_2 \in [0, 0.5]. \tag{8d}$$

The objective function Eq. (8a) rewards increasing intensities. The constraints Eq. (8b) ensure that the lasers operate at a steady state and the common frequency Ω. Equation (8c) represents the phase condition Eq. (5). The remaining constraints impose lower and upper bounds on the pump currents. We assume the first laser can dissipate more heat and therefore permits a higher pump current. The laser diodes are not identical, since different constraints Eq. (8d) apply to them. We anticipate the laser diodes are not identical in the subsequent examples. Note that this implies that symmetry cannot not be exploited to simplify an analysis.

The optimization Eq. (8) drives both pump currents towards their upper bounds,

$$p = [p_1, p_2]^T = [0.8, 0.5]^T. \tag{9}$$

This optimal point, which obviously results because the intensity increases with the pump currents, is illustrated in Fig. 2.

While the optimal point of operation Eq. (9) maximizes the intensity, it is of little use because it is not stable. This is illustrated with the time series shown in Fig. 3. After initialization in the state of synchronized operation ($t = 0$), the lasers operate with a common frequency Ω. At about $t = 1.8$, the synchronization is lost and the lasers start to operate chaotically. The loss of synchronization is spontaneous and is caused by the finite numerical precision in the simulation.

The result obtained in this section shows that a naive optimization may yield a point of operation that is optimal with respect to the objective function, but has unacceptable dynamical properties. This motivates to introduce constraints for stability and robustness. Specifically, we would like to

[1] The vector of uncertain variables is usually denoted α [25,27,30,35]. In the current paper, we use the symbol p instead to avoid a mix-up with the linewidth enhancement factor α.

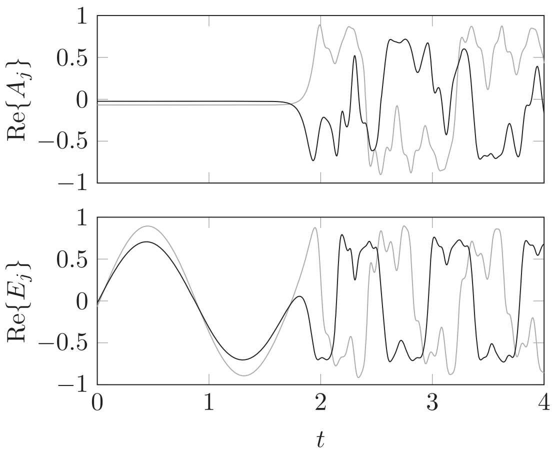

FIG. 3. Operation of the coupled lasers for the optimal parameters Eq. (9). Results are shown both in rotating coordinates A_j and original coordinates E_j.

ensure robust exponential stability of the synchronized state of Eq. (4).

C. Constraints on dynamical properties

Stability and robustness properties of optimal points of operation can be ensured by augmenting the optimization problem Eq. (8) by additional constraints. These constraints build on notions from applied bifurcation theory (see, e.g., Ref. [36]; see Ref. [25] for a concise description adapted to the use here). We first describe these constraints informally and then state technical details on the particular case treated here in Sec. II D.

Consider a nonlinear dynamical system with n_x state variables and n_p parameters. The system Eq. (4) with $n_x = 6$ and $n_p = 2$ may serve as an example. When starting at a stable steady state and varying one or more of the parameters quasistatically, the dynamical system will quasistatically move within its set of steady states. Simultaneously, the eigenvalues of the linearized dynamical system vary, and stable steady states turn into unstable ones when the leading eigenvalue crosses the imaginary axis into the right half of the complex plane. We refer to a point in parameter space at which a stable steady state turns into an unstable one, or, more generally, a steady state loses a desired property, as critical parameter value. Note that there may exist steady states beyond the critical values, which can be determined by solving the steady state equations even if it is not practical to operate the system at these values (due to instability, for example).

The set of steady states constitutes an n_p-dimensional manifold in the $(n_x + n_p)$-dimensional state-parameter space under mild conditions (see, e.g., Ref. [36, p. 429]). The critical parameter values constitute an $(n_p - 1)$-dimensional manifold, which is usually depicted after projecting it on the n_p-dimensional parameter space. Figure 4 shows a sketch of a two-dimensional parameter plane (i.e., $n_p = 2$) which is separated into an unstable and a stable region by a one-dimensional critical (i.e., $(n_p - 1)$-dimensional) manifold. The $(n_p - 1)$-dimensional manifolds of critical points can in general be described by systems of nonlinear equations of the form [25,26]

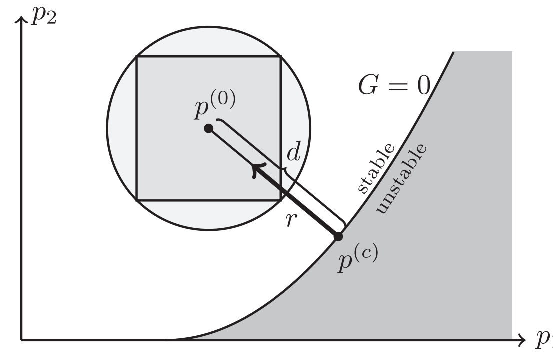

FIG. 4. The normal vector r connects $p^{(0)}$ to a closest critical parameter space point $p^{(c)}$ on the critical manifold defined by $G = 0$. The square represents Eq. (12).

$$G(x^{(c)}, p^{(c)}, u^{(c)}) = 0, \tag{10}$$

where $p^{(c)}$ and $x^{(c)}$ refer to the critical parameter value and the corresponding steady state and $u^{(c)}$ collects auxiliary variables. The specific equations G required in the present paper are stated in Sec. II D.

The distance of a stable point to the critical manifold can serve as a measure for robustness [26]. The shortest distance of a candidate point to the critical manifold occurs along a direction r that is normal to the critical manifold (see Fig. 4 for the sketch again). Just as the critical manifold can be characterized by Eq. (10), the normal vector can be calculated from a system of nonlinear equations of the form

$$H(x^{(c)}, p^{(c)}, u^{(c)}, v^{(c)}, r) = 0, \tag{11}$$

where $r \in \mathbb{R}^{n_p}$ is the normal vector and $v^{(c)}$ is short for additional auxiliary variables that appear in H but not in G. Normal vector systems Eq. (11) can be derived with a scheme given in Ref. [25]. The specific normal vector systems required in the present paper are given in Sec. II D and in the Appendices.

The normal vector r can now be used to state a constraint for robustness in optimization problems of the type Eq. (8) as follows [25]. Assume the parametric uncertainty of a dynamical system such as Eq. (4) can be described with uncertainty intervals. More precisely, assume the precise value of the parameters p is not known, but the elements of p are known to lie in intervals

$$p_i \in \left[p_i^{(0)} - \Delta p_i,\, p_i^{(0)} + \Delta p_i\right] \tag{12}$$

for $i = 1, \dots, n_p$, where Δp_i are known. If the parameters are scaled such that $\Delta p_i = 1$ for all i for convenience, then Eq. (12) defines an uncertainty hypercube (see Fig. 4 for a sketch for $n_p = 2$). All parameter values in this uncertainty hypercube can be guaranteed to lie in the stable region by enforcing the distance d in Fig. 4 to be larger than the radius $\sqrt{n_p}$ of the uncertainty hyperball that encloses the uncertainty hyperrectangle Eq. (12). This constraint can be expressed mathematically as

$$p^{(c)} = p^{(0)} + d\frac{r}{\|r\|}, \quad d > \sqrt{n_p}, \tag{13}$$

where the notation $r/\|r\|$ is used to point out that the normal vector has unit length.

By augmenting the optimization problem Eq. (8) with the constraints Eq. (13), robust stability can be ensured in the following sense: If there exists a steady state $x^{(0)}$ for parameters $p^{(0)}$ that obey Eq. (13), then $x^{(0)}$ is robust in that quasistatic variations of p around $p^{(0)}$ within Eq. (12) (the square in Fig. 4) will not cause the system to cross the critical manifold.

Note that more than one normal vector constraint may be necessary, because the robust region may be nonconvex, or because more than one critical manifold exists.

D. Constraints for robust exponential stability

The normal vector method summarized in the previous section has originally been developed to treat stability boundaries [25]. Local asymptotic stability of a steady state of the nonlinear system can be guaranteed by enforcing negative real parts of all eigenvalues of the linearized system at this steady state. While asymptotic stability can be guaranteed this way, the convergence to the steady state may become slow if eigenvalues exist very close to the imaginary axis. It is therefore of interest to generalize stability boundaries to critical boundaries for exponential stability to enforce a decay rate to the steady state. The decay rate, which can be specified by the user of the optimization method, is denoted σ below. We note that critical boundaries for exponential stability have first been treated in Ref. [28] for ordinary differential equations and in Ref. [32] delay differential equations.

The systems of equations $G=0$ and $H=0$ as introduced in Eqs. (10) and (11) for the characterization of these boundaries and the calculation of the normal to them, respectively, can be derived with the scheme proposed in Ref. [25]. We briefly summarize the resulting systems here as needed for the remainder of the paper. Technical details are deferred to the Appendix whenever possible to keep the explanations short.

For the general class of delay differential systems of the form Eqs. (6) and (7), the equations G and H introduced in Eqs. (10) and (11), respectively, read

$$f(\tilde{x}^{(c)}, \tilde{x}^{(c)}, \dots, \tilde{x}^{(c)}, p^{(c)}, \Omega^{(c)}) = 0, \tag{14a}$$

$$\sigma w - A_0^T w - \sum_{i=1}^{m} A_i^T \exp(-\sigma\tau_i)\, w = 0, \tag{14b}$$

$$w^T w - 1 = 0, \tag{14c}$$

$$\varphi(\tilde{x}^{(c)}, p^{(c)}, \Omega^{(c)}) = 0, \tag{14d}$$

$$\begin{bmatrix} \nabla_{\tilde{x}^{(c)}} f^T & B_{12}^{\mathrm{fold}} & 0 & \nabla_{\tilde{x}^{(c)}}\varphi \\ 0 & B_{32}^{\mathrm{fold}} & 2w & 0 \\ \nabla_{\Omega} f^T & B_{32}^{\mathrm{fold}} & 0 & \nabla_{\Omega^{(c)}}\varphi \end{bmatrix} \kappa = 0, \tag{14e}$$

$$\begin{bmatrix} \nabla_p f^T & B_{42}^{\mathrm{fold}} & 0 & \nabla_{p^{(c)}}\varphi \end{bmatrix} \kappa - r = 0, \tag{14f}$$

$$r^T r - 1 = 0, \tag{14g}$$

where A_0 and A_i refer to the Jacobians of f with respect to $x(t)$ and $x(t-\tau_i)$, $\sigma < 0$ is the desired decay rate and thus the critical value of the real parts of the eigenvalues, and the terms B_{ij}^{fold} are stated in the Appendices. Equations (14a)–(14d) constitute $G=0$ as introduced in Eq. (10), where Eq. (14a) enforce that $\tilde{x}^{(c)}$ for the critical parameter value $p^{(c)}$ is located on the steady state manifold, Eq. (14b) state that an eigenvalue with real part σ exists, Eq. (14c) is required to ensure regularity, and Eq. (14d) resolves the rotational symmetry. Equations (14e)–(14g) constitute $H=0$ as introduced in Eq. (11). Essentially, Eqs. (14e) and (14f) span the normal space to the critical manifold in the combined state-parameter space and select the particular normal vector that is normal to the state space (see Ref. [25] for details). Finally, Eq. (14g) normalizes r to unit length, which is required for $H=0$ to be regular.

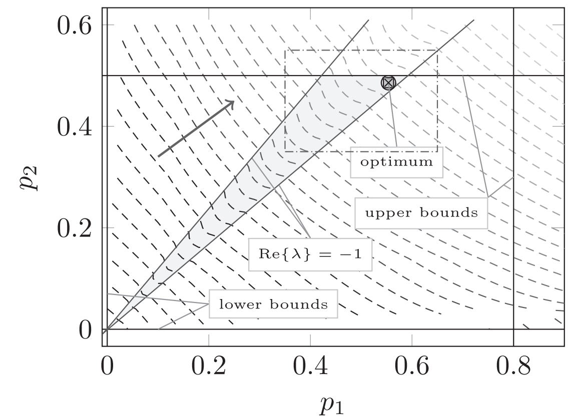

FIG. 5. Constraint geometry and optimum. Dashed lines are contour lines and represent the intensity $|A_1 + A_2|^2$, which ranges from 0 in the lower left corner to 2.9 in the upper right corner. The arrow points in the direction of increasing intensities. The maximal intensity is limited by the upper bound of p_2 and by a requirement of robust exponential stability. The interior of the dashdotted rectangle is shown in detail in Fig. 6.

We briefly note that Eqs. (14) generalizes G and H for the fold bifurcation. Fold bifurcations are characterized by a single real eigenvalue $\lambda = 0$ on the imaginary axis. Equations (14) extend the fold bifurcation case with $\lambda = 0$ to the case with $\lambda = \sigma$ for exponential stability [28,32]. Just as critical boundaries due to fold bifurcations have to be generalized to the exponential stability case, Hopf bifurcations, which are characterized by a complex conjugate pair of eigenvalues $\lambda = \pm i\omega$, must be generalized. The systems of equations for G and H for the Hopf case are stated in Eqs. (B1)–(B9) in the Appendices.

A robust optimal point can now be found using the normal vector systems introduced in this section. More precisely, the optimization problem Eq. (8) must be extended by Eq. (14) to calculate the normal to the critical manifold for exponential stability, and by Eq. (13) to enforce the desired robust distance from the critical manifold in the parameter space. The optimization result for a pump current uncertainty $\Delta p_i = 0.01$, $i = 1, 2$ and eigenvalue bound $\sigma = -1$ is shown in Figs. 5 and 6.

It is evident from Figs. 5 and 6 that two critical boundaries for exponential stability exist, one of which restricts the optimal point. Note that a normal vector constraint is also required to force the uncertainty ball into the halfspace $p_2 < 0.5$. In fact, normal vector systems can be stated for a large class of feasibility boundaries [25]. Due to the simplicity of the

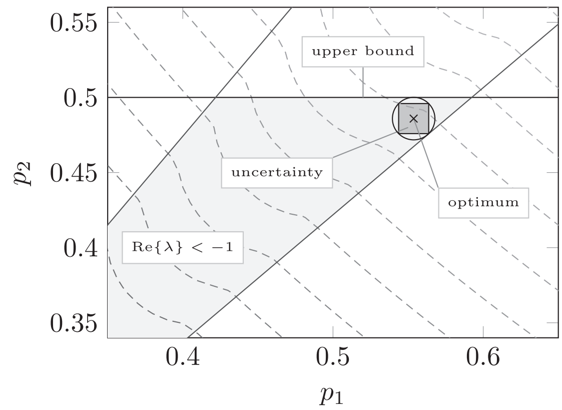

FIG. 6. Detailed view of the constraint geometry in Fig. 5. The robust exponential stability boundaries, the active upper bound, the quadratic uncertainty region and its circular outer approximation are shown.

boundary $p_2 < 0.5$, the constraint can be stated explicitly. It reads $p_2 < 0.5 - \sqrt{2}\Delta p_2 = 0.4859$.

The resulting optimal pump currents are

$$p = [p_1,\ p_2]^T = [0.5537,\ 0.4859]^T. \tag{15}$$

Figure 7 illustrates the optimization result with a simulation. The diodes are initialized in a nonsynchronized state at $t = 0$ and arrive at a steady state around $t = 1$. At the initial nonsynchronized state, the first laser diode is initialized at a 50% increased frequency and 24% increased electrical field, while the second laser diode is initialized with a 50% decreased frequency, both relative to the synchronized state. A more negative value of σ than $\sigma = -1$ chosen here would result in a faster synchronization speed. This value is respected in spite of the parameter uncertainty, which is shown in Fig. 8.

Finally, we stress that the critical boundaries need not to be known a priori, but can be detected in the course of the optimization with an approach that mimics an active set optimization method. We refer the reader to Ref. [35] for details.

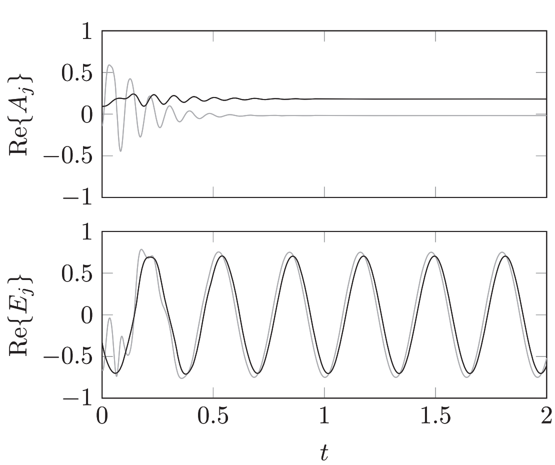

FIG. 7. Simulation of coupled lasers operating with pump currents Eq. (15). A_j shows synchronization as a steady state, E_j shows the electrical field in common fixed coordinates. The lasers synchronize.

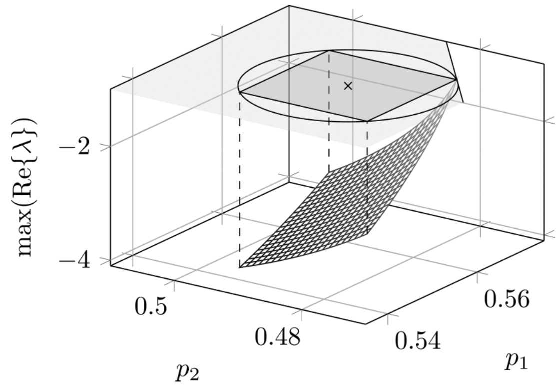

FIG. 8. The real parts of the leading eigenvalues are plotted against parameters within the uncertainty region. The largest eigenvalue real parts are found close to the critical manifold representing the required exponential stability.

III. OPTIMIZATION OF MULTIPLE COUPLED LASER DIODES

Having motivated the need for a robust optimization, we apply the method introduced in Sec. II to several laser diode networks. The networks treated in Secs. III A and III B involve three uncertain parameters. The results for these two cases can therefore be visualized and, at least in principle, the robust optimal points could be determined by an elaborate visual analysis of critical manifolds and level sets of the objective function. This is no longer the case for the third example, which has ten uncertain parameters. The third example demonstrates that the proposed robust optimization method can be applied to systems for which a visual analysis is no longer practical.

A. Three symmetrically coupled laser diodes

The system shown in Fig. 9 is a straight forward extension of the laser network in Sec. II. The delay differential equations for this network read

$$\frac{1}{\theta}\dot{A}_j(t) = -\mathrm{i}\Omega A_j(t) + (1 + \mathrm{i}\alpha)n_j(t)A_j(t) + \sum_{k=1}^{3}\eta_{jk}\mathrm{e}^{\mathrm{i}(\phi-\Omega\tau)}A_k(t-\tau), \tag{16a}$$

$$\frac{1}{\theta}\dot{n}_j(t) = \epsilon\{p_j - n_j(t) - [2n_j(t)+1]|A_j(t)|^2\}, \tag{16b}$$

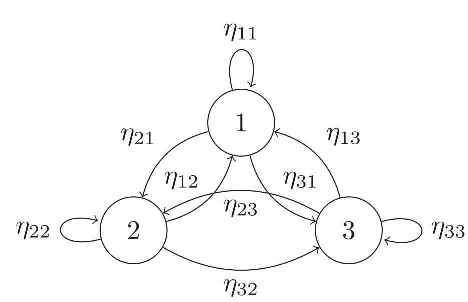

FIG. 9. Coupling structure of three symmetrically coupled lasers.

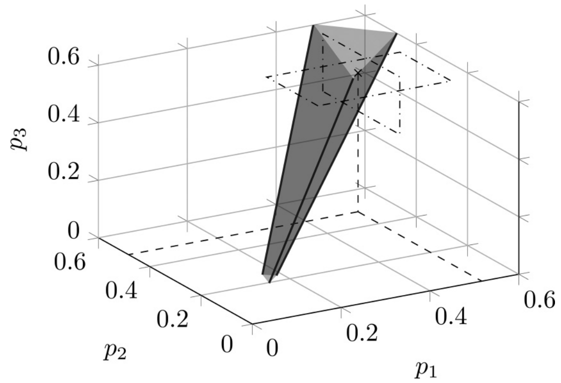

FIG. 10. Exponential stability boundaries and optimal point for the network from Fig. 9. Points in the interior of the cone have the required exponential stability. The dashdotted rectangles indicate the cuts shown in Figs. 11 and 12.

where $j = 1, \ldots, 3$. The coupling coefficients are set to $\eta_{jk} = 0.00167$ for $j, k = 1, 2, 3$.

We assume the first laser can dissipate more heat than the other two. This is modeled by setting the pump current bounds to

$$p_1 \in [0, 0.8], \quad p_2 \in [0, 0.5], \quad p_3 \in [0, 0.5]. \tag{17}$$

We intend to maximize the combined intensity of this network. The objective function therefore reads $-|\sum_{j=1}^{3} A_j|^2$. Simultaneously, we want to ensure synchronization with a decay rate $\sigma = -1$ and satisfaction of the constraints Eq. (17) on the pump currents for an uncertainty of $\Delta p_i = 0.01$.

The result of the optimization is shown in Fig. 10. Three critical points must be taken into account that all are of the modified fold type and can therefore be described with Eq. (14). The critical boundaries for exponential stability are highlighted in Fig. 10.

The resulting optimal pump currents are

$$[p_1, p_2, p_3]^T = [0.5167, 0.4827, 0.4827]^T. \tag{18}$$

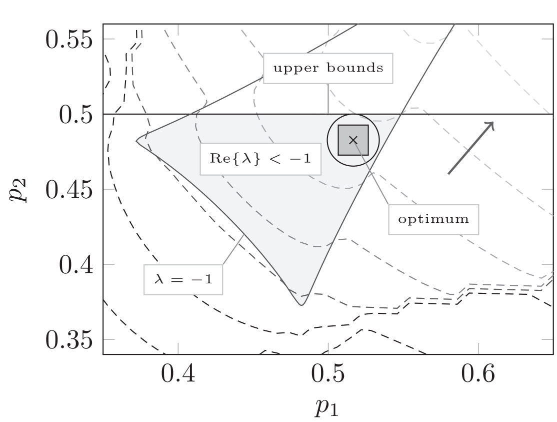

FIG. 11. p_1-p_2 plane of three symmetrically coupled lasers: The active upper bound and the modified fold manifolds are visible and labeled. Contour lines are dashed and indicate the intensity ranging from 1.85 in the lower left corner to 2.2 in the upper right corner. The arrow points toward increasing intensities.

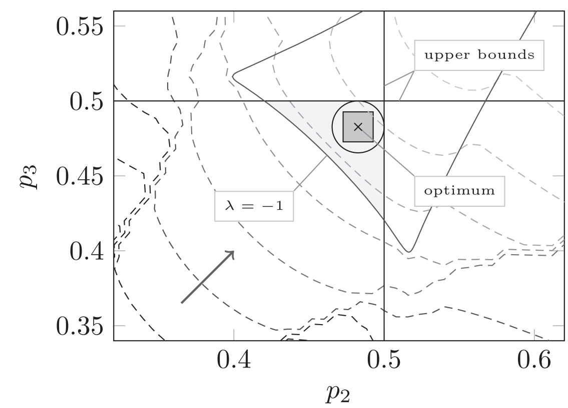

FIG. 12. p_2-p_3 plane of three symmetrically coupled lasers: All active constraints are visible and labeled. The depicted intensity ranges from 1.75 in the lower left corner to 2.25 in the upper right corner. The arrow points toward increasing intensities.

The upper bounds on p_2 and p_3 are active at the optimum and so is one exponential stability boundary. The results are visualized in Figs. 11 and 12, which show a cut at $p_3 = 0.4827$ and a cut at $p_1 = 0.5167$. All active constraints are visible in Fig. 12, although the exponential stability boundary (labeled with $\lambda = -1$) appears not to touch the spherical uncertainty region. This is caused by the placement of the cut. The contact point of exponential stability boundary and uncertainty region is at $p_1 = 0.5303$, which is outside the cut. Note that it is evident from Fig. 12 that even for three uncertain parameters, it would be difficult to find the robust optimum based on visualizations.

Simulation results for this optimum are plotted in Fig. 13. All lasers suffer from a disturbance at $t = 0$. The electrical fields differ up to 20% from their synchronized state electrical fields. Their initial frequencies vary in the range of $\pm 50\%$, based on their synchronized frequency. They quickly synchronize. A more negative value than $\sigma = -1$ would have resulted in a faster decay to the synchronized state but a lower value for the optimal intensity.

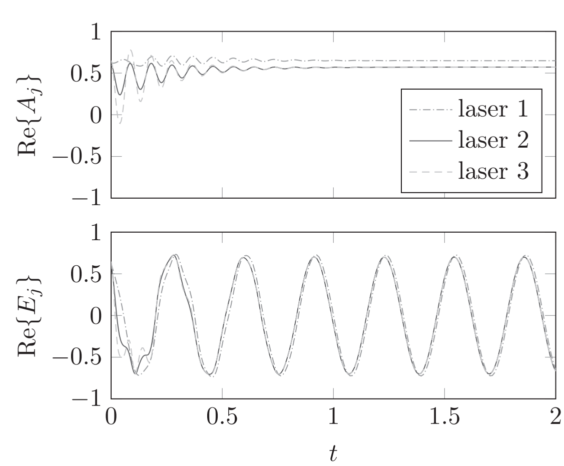

FIG. 13. Three symmetrically coupled lasers at optimum Eq. (18). A_j shows synchronization as a steady state, E_j shows the electrical field in common fixed coordinates. The lasers synchronize.

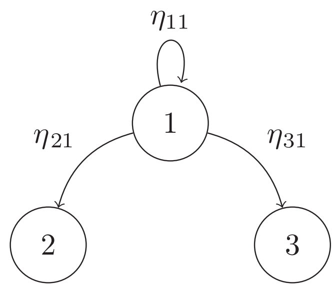

FIG. 14. Coupling structure of three asymmetrically coupled lasers. The goal is that lasers 2 and 3 synchronize with laser 1, but do not interact with each other.

B. Three hierarchically coupled laser diodes

The next laser network to be optimized is one with a hierarchical structure that is shown in Fig. 14. This hierarchical network does not allow any bidirectional interaction between laser diodes. The first laser alone determines the frequency of the laser network. The other lasers have to synchronize without being able to influence the frequency in any way. Such a laser network would be much easier to trim for a desired frequency because local disturbances remain local.

The differential equations for this laser network are the same as in Eq. (16). The differences in the structure can be accounted for by adjusting the coupling coefficients η_{jk}. They read $\eta_{11} = \eta_{21} = \eta_{31} = 0.005$ here. All remaining coefficients $\eta_{j2}, \eta_{j3}, j = 1, \ldots, 3$ are zero.

Due to the laser's different properties, the first laser will contribute a larger part of its output to the other lasers, therefore the out-bound coupling coefficients of laser 1 are $\eta_{j1} = 0.005$. The out-bound coupling coefficients of lasers 2 and 3 vanish, $\eta_{j2} = 0$ and $\eta_{j3} = 0$. The bounds on the pump currents read

$$p_1 \in [0, 0.8], \quad p_2 \in [0, 0.7], \quad p_3 \in [0, 0.4], \tag{19}$$

in this case. The upper bounds on the pump currents p_2 and p_3 are set to different values to break the symmetry. The objective function $-|\sum_{j=1}^{3} A_j|^2$, the decay rate $\sigma = -1$ and

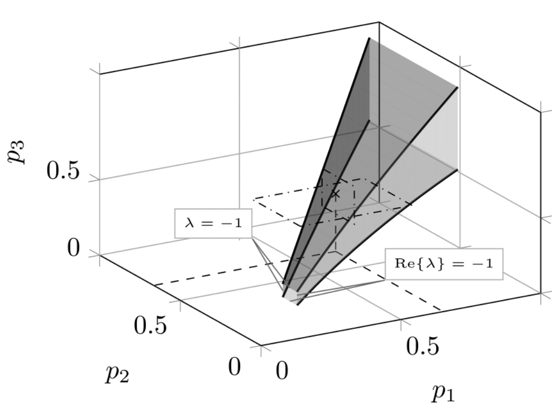

FIG. 15. Exponential stability boundaries and optimal point for the network from Fig. 14. Points in the interior of the cone have the required stability properties. The dash-dotted rectangles indicate the cuts shown in Figs. 16 and 17.

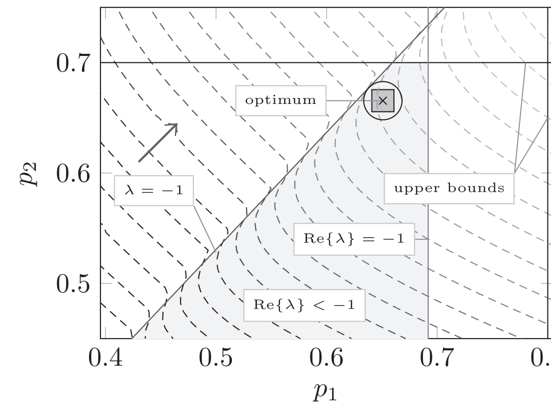

FIG. 16. p_1-p_2 plane of three hierarchically coupled lasers at the optimum: active boundaries of both types (real eigenvalue $\lambda = \sigma$ and complex conjugated eigenvalue pair with $\mathrm{Re}\{\lambda\} = \sigma$) are visible and labeled. The dashed contour lines depict intensities ranging from 1.9 in the lower left corner to 2.34 in the upper right corner. The arrow points toward increasing intensities.

the uncertainties $\Delta p_i = 0.01$, $i = 1, \ldots, 3$ are chosen as in the previous example.

Figure 15 shows the optimization result in the space of the pump currents. Two critical boundaries of the modified fold type (darker facets) and two critical boundaries of the modified Hopf type (lighter facets) exist. The optimal pump currents are

$$[p_1, p_2, p_3]^T = [0.5943, 0.6061, 0.3827]^T. \tag{20}$$

The upper bound on p_3, one normal vector constraint for a modified fold boundary and a modified Hopf boundary are active at the optimal point. The results are visualized in Figs. 16 and 17.

A simulation with optimal pump currents is shown in Fig. 18. The simulation starts at $t = 0$ with laser 1 in its steady state, while lasers 2 and 3 are disturbed and their electrical fields are elevated by 30% and 20%, respectively. The initial

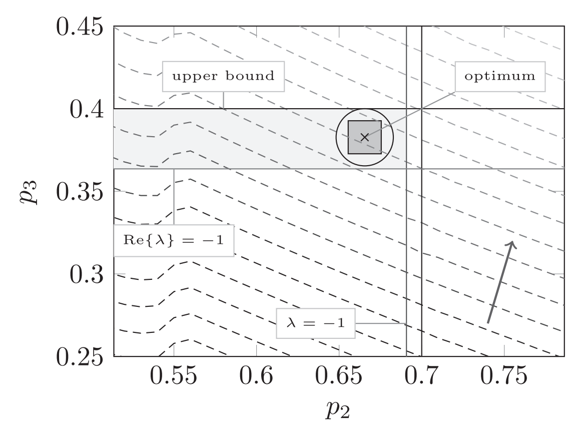

FIG. 17. p_2-p_3 plane of three hierarchically coupled lasers at the optimum: All active constraints are visible and labeled (cf. Fig. 16). The intensity is depicted by dashed lines, it ranges from 1.88 in the lower left corner to 2.26 in the upper right corner. The arrow points toward increasing intensities.

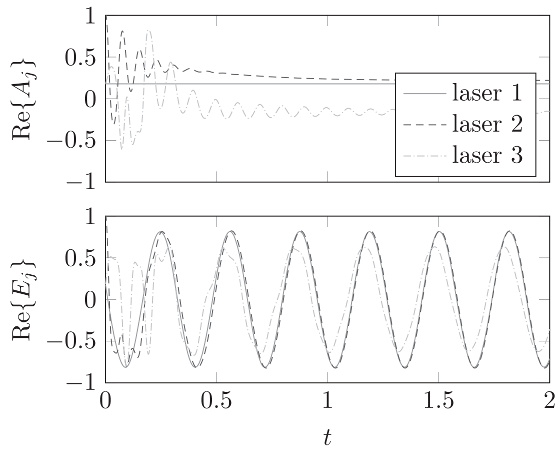

FIG. 18. Simulation of hierarchically coupled lasers at optimum Eq. (20). A_j shows synchronization as a steady state, E_j shows the electrical field in common fixed coordinates. The lasers synchronize.

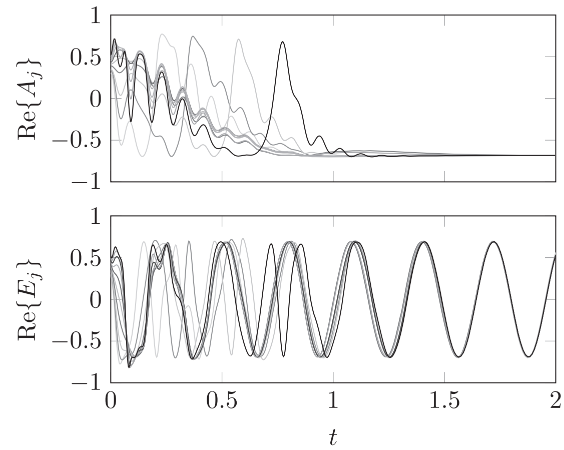

FIG. 19. Ten symmetrically coupled lasers at optimum Eq. (22). A_j shows synchronization as a steady state, E_j shows the electrical field in common fixed coordinates. The lasers synchronize.

frequency of laser 2 is 50% lower, the frequency of laser 3 is 30% higher, relative to laser 1. This scenario was intentionally chosen because it emphasizes the benefits of the network structure. Lasers 2 and 3 can influence neither each other nor laser 1. Nevertheless, the lasers quickly synchronize. The rate of decay to the synchronized state can be controlled with σ.

C. Ten coupled laser diodes

The last example demonstrates that the proposed robust optimization method is suitable for large problems. While the previous examples could arguably have been optimized by hand, i.e., graphical analysis of the critical boundaries carried out by a skilled person, the example treated here requires a systematic and automatic method.

The network treated in this section consists of ten laser diodes and, consequently, is described by a total of thirty states ($n_x = 30$) and one algebraic variable (the coordinate rotation frequency Ω). There are $n_p = 10$ uncertain parameters (pump currents p_1 to p_{10}). We anticipate that ten different exponential stability boundaries of the modified fold type appear in the optimization problem, each of which requires $4n_x + 2n_p + 3 = 143$ equations to describe both, boundary and normal vector. In summary, the optimization problem has 1481 optimization variables, 1461 equality constraints, and 10 inequality constraints and uncertain parameters.

The model Eqs. (4) need to be extended to the case with ten diodes. This results in

$$\frac{1}{\theta}\dot{A}_j(t) = -\mathrm{i}\Omega A_j(t) + (1+\mathrm{i}\alpha)n_j(t)A_j(t) + \sum_{k=1}^{10}\eta_{jk}\mathrm{e}^{\mathrm{i}(\phi-\Omega\tau)}A_k(t-\tau), \tag{21a}$$

$$\frac{1}{\theta}\dot{n}_j(t) = \epsilon\{p_j - n_j(t) - [2n_j(t)+1]|A_j(t)|^2\}, \tag{21b}$$

for $j = 1,\ldots,10$. Accordingly, the objective function for maximum intensity now reads $-|\sum_{j=1}^{10} A_j|^2$. We assume symmetric coupling with coupling coefficients $\eta_{jk} = 0.5\times10^{-3}$ for $j,k = 1,\ldots,10$. The bounds on the pump currents are set to

$$p_j \in [0, 0.8] \quad \text{for } j = 1,\ldots,3, \tag{21c}$$

$$p_j \in [0, 0.5] \quad \text{for } j = 4,\ldots,10. \tag{21d}$$

We choose these bounds to model a triangular or pyramidal arrangement of the laser diodes on the semiconductor. The laser diodes in the corners can dissipate heat more easily, and therefore can bear larger pump currents. The uncertainty of the pump currents $\Delta p_j = 0.01$, $j = 1,\ldots,10$ and the bound $\sigma = -1$ are as before.

The robust optimization results in the optimal pump currents

$$\begin{bmatrix} p_1\\ p_2\\ p_3\\ p_4\\ p_5\\ p_6\\ p_7\\ p_8\\ p_9\\ p_{10}\end{bmatrix} = \begin{bmatrix} 0.4813\\ 0.4749\\ 0.4774\\ 0.4684\\ 0.4684\\ 0.4684\\ 0.4684\\ 0.4684\\ 0.4684\\ 0.4684\end{bmatrix}. \tag{22}$$

The upper bounds in Eqs. (21d) and one normal vector constraint are active at the optimum. Due to the high dimension, a graphic representation of the optimal point, as carried out in the previous examples, is no longer possible. A simulation of the synchronization of ten laser diodes at the optimum is shown in Fig. 19. The simulation starts at $t = 0$ with a disturbance and therefore without synchronization. Compared to the synchronized state, the electrical fields are larger by up to 30%, while the frequencies vary up to ±50%.

Convergence to the synchronized state is slower than for the previous examples, but the synchronized state is reached at about $t = 1.5$.

IV. CONCLUSION

We showed that optimal, open-loop stable and robust points of operation of laser networks can systematically be found with the normal vector method. Essentially, robustness is achieved by surrounding the candidate optimal point of optimization with an uncertainty region in the parameter space. The resulting optimal point is then guaranteed to remain stable despite uncertainty in the pump currents. Furthermore, we showed that it is straight forward to extend the method for guaranteeing exponential stability with a user-specified rate. This rate can be used to tune the convergence to the synchronized state in the laser networks.

The optimized coupling configurations included symmetric as well as hierarchical coupling structures and different system sizes, ranging from a laser network with two laser diodes and six state variables to a network with 10 lasers, 30 state variables, and 1481 optimization variables. This corroborates that the proposed method can be applied to nontrivial networks.

ACKNOWLEDGMENT

Funding by Deutsche Forschungsgemeinschaft (Grant No. MO 1086/13-1) is gratefully acknowledged.

APPENDIX A: NORMAL VECTOR SYSTEM FOR MODIFIED FOLD BIFURCATIONS

The expressions for B_{ij}^{fold} introduced in Eq. (14) read as follows:

$$\begin{aligned}
B_{12}^{\text{fold}} &= -\sum_{i=0}^{m} \exp(-\sigma\tau_i)\nabla_{\tilde{x}^{(c)}}(w^T A_i) \\
&\quad + \sigma\sum_{i=0}^{m} w^T A_i \exp(-\sigma\tau_i)\nabla_{\tilde{x}^{(c)}}\tau_i, \\
B_{22}^{\text{fold}} &= \sigma I - \sum_{i=0}^{m} A_i \exp(-\sigma\tau_i), \\
B_{32}^{\text{fold}} &= -\sum_{i=0}^{m} \exp(-\sigma\tau_i)\nabla_{\Omega}(w^T A_i), \\
B_{42}^{\text{fold}} &= -\sum_{i=0}^{m} \exp(-\sigma\tau_i)\nabla_{p^{(c)}}(w^T A_i) \\
&\quad + \sigma\sum_{i=0}^{m}(\nabla_{p^{(c)}}\tau_i)[\exp(-\sigma\tau_i)\, w^T]A_i^T.
\end{aligned}$$

Equations (14a)–(14d), which constitute $G = 0$ as introduced in Eq. (10), comprise $2n_x + 2$ equations that are regular in the $2n_x + 2$ variables $\tilde{x}^{(c)}$, w, Ω and one of the parameters $p_i^{(c)}$, where all other parameters $p_j^{(c)}$, $i \neq j$ are fixed.

APPENDIX B: NORMAL VECTOR SYSTEMS FOR MODIFIED HOPF BIFURCATIONS

A Hopf bifurcation occurs if a leading pair of complex conjugate eigenvalues with nonzero imaginary part transversally crosses the imaginary axis into the right half of the complex plane under parameter variations (see, e.g., Ref. [36, p. 93]), in particular, $\sigma = 0$ at a Hopf bifurcation. We are interested in critical points defined by values $\sigma < 0$, where σ can be specified by the user of the optimization method in order to achieve a desired decay rate. In analogy to the well-known necessary conditions for a Hopf bifurcation, the following system $G = 0$ can be stated for the modified Hopf bifurcation point with $\sigma < 0$:

$$f(\tilde{x}^{(c)}, \tilde{x}^{(c)}, \ldots, \tilde{x}^{(c)}, p^{(c)}, \Omega) = 0, \tag{B1}$$

$$\sigma a - \omega b - \sum_{i=0}^{m} A_i[\mathrm{c}(\lambda, \tau_i)a + \mathrm{s}(\lambda, \tau_i)b] = 0, \tag{B2}$$

$$\omega a + \sigma b - \sum_{i=0}^{m} A_i[\mathrm{c}(\lambda, \tau_i)b - \mathrm{s}(\lambda, \tau_i)a] = 0, \tag{B3}$$

$$a^T a + b^T b - 1 = 0, \tag{B4}$$

$$a^T b = 0, \tag{B5}$$

$$\varphi(\tilde{x}^{(c)}, p^{(c)}, \Omega^{(c)}) = 0. \tag{B6}$$

Here, $\tau_0 = 0$, $\mathrm{c}(\lambda, \tau_i) = \exp(-\sigma\tau_i)\cos(\omega\tau_i)$, and $\mathrm{s}(\lambda, \tau_i) = \exp(-\sigma\tau_i)\sin(\omega\tau_i)$, Eq. (B1) ensures that $\tilde{x}^{(c)}$ is a steady state for the parameter values $p^{(c)}$, and Eqs. (B2) and (B3) enforce that there exists an eigenvalue pair $\sigma \pm \mathrm{i}\omega$. The remaining two equations ensure that Eqs. (B1)–(B6) is a regular system of $3n_x + 3$ equations for $\tilde{x}^{(c)}$, a, b, ω, Ω and one of the parameters $p_i^{(c)}$, where the remaining parameters $p_j^{(c)}$, $j \neq i$, and σ are fixed.

When Eqs. (B1)–(B6) are extended by the following equations, the normal vector system $H = 0$ results:

$$\begin{bmatrix}
\nabla_{\tilde{x}^{(c)}} f^T & B_{12}^{\text{Hopf}} & B_{13}^{\text{Hopf}} & 0 & 0 & \nabla_{\tilde{x}^{(c)}}\varphi \\
0 & B_{22}^{\text{Hopf}} & B_{23}^{\text{Hopf}} & 2a & b & 0 \\
0 & B_{32}^{\text{Hopf}} & B_{33}^{\text{Hopf}} & 2b & a & 0 \\
0 & B_{42}^{\text{Hopf}} & B_{43}^{\text{Hopf}} & 0 & 0 & 0 \\
\nabla_{\Omega^{(c)}} f^T & B_{52}^{\text{Hopf}} & B_{53}^{\text{Hopf}} & 0 & 0 & \nabla_{\Omega^{(c)}}\varphi \\
 & & & & &
\end{bmatrix}\kappa = 0, \tag{B7}$$

$$[\nabla_{p^{(c)}} f^T \quad B_{62}^{\text{Hopf}} \quad B_{63}^{\text{Hopf}} \quad 0 \quad 0 \quad \nabla_{p^{(c)}}\varphi]\kappa - r = 0, \tag{B8}$$

$$r^T r - 1 = 0. \tag{B9}$$

The expressions for B_{ij}^{Hopf} are stated below. Essentially, Eqs. (B7) and (B8) determine that the normal direction to the manifold of modified Hopf points in the space of the uncertain parameters [25]. The last equation is required to normalize the normal vector to unit length. The matrices B_{ij}^{Hopf} read as follows:

$$
\begin{aligned}
B_{12}^{\text{Hopf}} = & \sum_{i=0}^{m} \sigma(\nabla_{\tilde{x}^{(c)}}\tau_i)[\mathrm{c}(\lambda,\tau_i)a^T + \mathrm{s}(\lambda,\tau_i)b^T]A_i^T \\
& - \sum_{i=0}^{m} \omega(\nabla_{\tilde{x}^{(c)}}\tau_i)[\mathrm{c}(\lambda,\tau_i)b^T - \mathrm{s}(\lambda,\tau_i)a^T]A_i^T \\
& - \sum_{i=0}^{m} \mathrm{c}(\lambda,\tau_i)\big(\nabla_{\tilde{x}^{(c)}}a^T A_i^T\big) + \mathrm{s}(\lambda,\tau_i)\big(\nabla_{\tilde{x}^{(c)}}b^T A_i^T\big), \\
B_{13}^{\text{Hopf}} = & \sum_{i=0}^{m} \sigma(\nabla_{\tilde{x}^{(c)}}\tau_i)[\mathrm{c}(\lambda,\tau_i)b^T - \mathrm{s}(\lambda,\tau_i)a^T]A_i^T \\
& + \sum_{i=0}^{m} \omega(\nabla_{\tilde{x}^{(c)}}\tau_i)[\mathrm{s}(\lambda,\tau_i)b^T + \mathrm{c}(\lambda,\tau_i)a^T]A_i^T \\
& - \sum_{i=0}^{m} \mathrm{c}(\lambda,\tau_i)\big(\nabla_{\tilde{x}^{(c)}}b^T A_i^T\big) - \mathrm{s}(\lambda,\tau_i)\big(\nabla_{\tilde{x}^{(c)}}a^T A_i^T\big), \\
B_{22}^{\text{Hopf}} = & \,\sigma I - \sum_{i=0}^{m} \mathrm{c}(\lambda,\tau_i)A_i^T, \\
B_{23}^{\text{Hopf}} = & \,\omega I + \sum_{i=0}^{m} \mathrm{s}(\lambda,\tau_i)A_i^T, \\
B_{32}^{\text{Hopf}} = & -\omega I - \sum_{i=0}^{m} \mathrm{s}(\lambda,\tau_i)A_i^T, \\
B_{33}^{\text{Hopf}} = & \,\sigma I - \sum_{i=0}^{m} \mathrm{c}(\lambda,\tau_i)A_i^T, \\
B_{42}^{\text{Hopf}} = & -b^T + \sum_{i=0}^{m} \tau_i[\mathrm{s}(\lambda,\tau_i)a^T - \mathrm{c}(\lambda,\tau_i)b^T)]A_i^T, \\
B_{43}^{\text{Hopf}} = & \,a^T + \sum_{i=0}^{m} \tau_i[\mathrm{s}(\lambda,\tau_i)b^T + \mathrm{c}(\lambda,\tau_i)a^T)]A_i^T, \\
B_{52}^{\text{Hopf}} = & -\sum_{i=0}^{m} \mathrm{c}(\lambda,\tau_i)\big(\nabla_{\Omega}a^T A_i^T\big) + \mathrm{s}(\lambda,\tau_i)\big(\nabla_{\Omega}b^T A_i^T\big), \\
B_{53}^{\text{Hopf}} = & -\sum_{i=0}^{m} \mathrm{c}(\lambda,\tau_i)\big(\nabla_{\Omega}b^T A_i^T\big) - \mathrm{s}(\lambda,\tau_i)\big(\nabla_{\Omega}a^T A_i^T\big), \\
B_{62}^{\text{Hopf}} = & \sum_{i=0}^{m} \sigma(\nabla_{p^{(c)}}\tau_i)[\mathrm{c}(\lambda,\tau_i)a^T + \mathrm{s}(\lambda,\tau_i)b^T]A_i^T \\
& + \sum_{i=0}^{m} \omega(\nabla_{p^{(c)}}\tau_i)[\mathrm{s}(\lambda,\tau_i)a^T - \mathrm{c}(\lambda,\tau_i)b^T]A_i^T \\
& - \sum_{i=0}^{m} \mathrm{c}(\lambda,\tau_i)\big(\nabla_{p^{(c)}}a^T A_i^T\big) + \mathrm{s}(\lambda,\tau_i)\big(\nabla_{p^{(c)}}b^T A_i^T\big), \\
B_{63}^{\text{Hopf}} = & \sum_{i=0}^{m} \sigma(\nabla_{p^{(c)}}\tau_i)[\mathrm{c}(\lambda,\tau_i)b^T - \mathrm{s}(\lambda,\tau_i)a^T]A_i^T \\
& + \sum_{i=0}^{m} \omega(\nabla_{p^{(c)}}\tau_i)[\mathrm{s}(\lambda,\tau_i)b^T + \mathrm{c}(\lambda,\tau_i)a^T]A_i^T \\
& - \sum_{i=0}^{m} \mathrm{c}(\lambda,\tau_i)\big(\nabla_{p^{(c)}}b^T A_i^T\big) - \mathrm{s}(\lambda,\tau_i)\big(\nabla_{p^{(c)}}a^T A_i^T\big).
\end{aligned}
$$

The expressions $\nabla_{\tilde{x}^{(c)}}a^T A_i^T$ are given by

$$\big(\nabla_{\tilde{x}^{(c)}}a^T A_i^T\big)_{\mu,\nu} = \sum_{\rho=1}^{n} a_\rho \frac{\partial^2 f_\nu}{\partial \tilde{x}_\mu^{(c)}\, \partial \tilde{x}_\rho^{(c)}(t-\tau_i)}.$$

The expressions $\nabla_{\tilde{x}^{(c)}}b^T A_i^T$, $\nabla_{p^{(c)}}a^T A_i^T$, and $\nabla_{p^{(c)}}b^T A_i^T$ are defined accordingly.

[1] G. P. Agrawal and N. Dutta, *Semiconductor Lasers* (Kluwer Academic Publishers, Dordrecht, 1993).

[2] R. Lang and K. Kobayashi, IEEE J. Quant. Electron. **QE-16**, 347 (1980).

[3] G. P. Agrawal, J. Appl. Phys. **56**, 3100 (1984).

[4] K. Verheyden, K. Green, and D. Roose, Phys. Rev. E **69**, 036702 (2004).

[5] P. M. Alsing, V. Kovanis, A. Gavrielides, and T. Erneux, Phys. Rev. A **53**, 4429 (1996).

[6] V. Flunkert and E. Schöll, New J. Phys. **14**, 033039 (2012).

[7] B. Haegeman, K. Engelborghs, D. Roose, D. Pieroux, and T. Erneux, Phys. Rev. E **66**, 046216 (2002).

[8] T. Heil, I. Fischer, W. Elsäßer, B. Krauskopf, K. Green, and A. Gavrielides, Phys. Rev. E **67**, 066214 (2003).

[9] V. Rottschäfer and B. Krauskopf, Int. J. Bifurcation Chaos Appl. Sci. Eng. **17**, 1575 (2007).

[10] V. Flunkert, *Delay-Coupled Complex Systems and Applications to Lasers* (Springer, Berlin, 2011).

[11] M. Sciamanna and K. A. Shore, Nat. Photon. **9**, 151 (2015).

[12] D. R. Scifres, W. Streifer, and R. D. Burnham, IEEE J. Quant. Electron. **QE-15**, 917 (1979).

[13] K. Green, B. Krauskopf, and G. Samaey, SIAM J. Appl. Dyn. Syst. **2**, 254 (2003).

[14] J. Sieber, K. Engelborghs, T. Luzyanina, G. Samaey, and D. Roose, DDE-BIFTOOL v. 3.0 Manual—Bifurcation Analysis of Delay Differential Equations (2014), https://arxiv.org/pdf/1406.7144v2.pdf.

[15] "Demo of extension for rotational symmetry using Lang-Kobayashi equations", http://ddebiftool.sourceforge.net/demos/rotsym_demo/html/rotsym_demo.html.

[16] I. V. Ermakov, G. V. der Sande, and J. Danckaert, Commun. Nonlinear Sci. Numer. Simul. **17**, 4767 (2012).

[17] G. Kozyreff, A. G. Vladimirov, and P. Mandel, Phys. Rev. Lett. **85**, 3809 (2000).

[18] G. Kozyreff, A. G. Vladimirov, and P. Mandel, Phys. Rev. E **64**, 016613 (2001).

[19] D. Bertsekas, *Nonlinear Programming* (Athena Scientific, Nashua, NH, 2016).

[20] M. Ehrgott, *Multicriteria Optimization*, Lecture Notes in Economics and Mathematical Systems (Springer, Berlin, 2005).

[21] J. Vanbiervliet, K. Verheyden, W. Michiels, and S. Vandewalle, ESAIM Control Optim. Calc. Var. **14**, 478 (2008).

[22] Y. C. Kouomou and P. Woafo, Phys. Rev. E **67**, 026214 (2003).
[23] S. Priyadarshi, I. Pierce, Y. Hong, and K. A. Shore, Semicond. Sci. Technol. **27**, 094002 (2012).
[24] L. Fenzi and W. Michiels, Linear Algebra Appl. **526**, 1 (2017).
[25] M. Mönnigmann and W. Marquardt, J. Nonlinear Sci. **12**, 85 (2002).
[26] I. Dobson, J. Nonlinear Sci. **3**, 307 (1993).
[27] J. Gerhard, M. Mönnigmann, and W. Marquardt, SIAM J. Appl. Dyn. Syst. **7**, 461 (2008).
[28] D. Kastsian and M. Mönnigmann, SIAM J. Appl. Dyn. Syst. **9**, 357 (2010).
[29] D. Kastsian and M. Mönnigmann, IFAC Proc. Vol. **46**, 433 (2013).
[30] D. Kastsian and M. Mönnigmann, Chem. Eng. Sci. **106**, 109 (2014).
[31] J. Otten and M. Mönnigmann, in *Proceedings of the 55th IEEE Conference on Decision and Control* (IEEE, Las Vegas, NV, 2016), pp. 1441–1446.
[32] J. Otten and M. Mönnigmann, IFAC-PapersOnLine **49**, 47 (2016).
[33] A. Hohl and A. Gavrielides, Phys. Rev. Lett. **82**, 1148 (1999).
[34] B. Krauskopf, G. van Tartwijk, and G. Gray, Opt. Commun. **177**, 347 (2000).
[35] M. Mönnigmann, W. Marquardt, C. H. Bischof, T. Beelitz, B. Lang, and P. Willems, SIAM Rev. **49**, 236 (2007).
[36] J. A. Kuznetsov, *Elements of Applied Bifurcation Theory*, 2nd ed., Applied Mathematical Sciences (Springer, New York, 1998), Vol. 112.